

InAs/GaAs pyramidal quantum dots: Strain distribution, optical phonons, and electronic structure

M. Grundmann,* O. Stier, and D. Bimberg

Institut für Festkörperphysik, Technische Universität Berlin, Hardenbergstraße 36, D-10623 Berlin, Germany

(Received 17 April 1995)

The strain distribution in and around pyramidal InAs/GaAs quantum dots (QD's) on a thin wetting layer fabricated recently with molecular-beam epitaxy, is simulated numerically. For comparison analytical solutions for the strain distribution in and around a pseudomorphic slab, cylinder, and sphere are given for isotropic materials, representing a guideline for the understanding of strain distribution in two-, one-, and zero-dimensional pseudomorphic nanostructures. For the pyramidal dots we find that the hydrostatic strain is mostly confined in the QD; in contrast part of the anisotropic strain is from the QD into the barrier. The optical-phonon energies in the QD are estimated and agree perfectly with recent experimental findings. From the variation of the strain tensor the local band-gap modification is calculated. Piezoelectric effects are additionally taken into account. The three-dimensional effective-mass single-particle Schrödinger equation is solved for electrons and holes using the realistic confinement potentials. Since the QD's are in the strong confinement regime, the Coulomb interaction can be treated as a perturbation. The thus obtained electronic structure agrees with luminescence data. Additionally AlAs barriers are considered.

I. INTRODUCTION

Structures are called pseudomorphic when they are lattice mismatched to their substrate, and the strain is accommodated entirely elastically without plastic relaxation via crystal defects, e.g., dislocations. Pseudomorphic systems have attracted immense interest due to their unique potential to exhibit novel electronic and device properties via use of a wealth of mismatched material combinations.¹ Originally, strained semiconductor quantum wells had been proposed and demonstrated to yield improved laser performance.² Recently, pseudomorphic quantum wires and quantum dots (QD's) have emerged as exciting realizations of one- and zero-dimensional mismatched systems. For self-organized quantum dots realized via Stranski-Krastanov growth, strain is actually the driving force for the creation of dots.³

In this paper we present a thorough investigation of the strain distribution in and around self-organized InAs/GaAs quantum dots, whose pyramidal shape has been evidenced by high-resolution transmission electron microscopy.⁴ The base sides of the pyramids are oriented along [100] and [010], and the side facets are close to {011}. The typical base length is $b=12$ nm, with a height of 6 nm. Due to the Stranski-Krastanov growth mode, the dots reside on a continuous wetting layer (WL) whose thickness L is in the monolayer (ML) regime. Numerical results for the strain distribution are obtained by minimizing the total strain energy of the quantum dot, wetting layer and barrier. The modification of LO-phonon energy by strain in the pyramidal QD's is estimated and found to agree with recent experiments.⁵ In the actual confinement potential, modified by the strain and piezoelectric effects, we solve numerically the three-dimensional effective-mass Schrödinger equation and ob-

tain the realistic electronic structure and wave functions of the QD's. Coulomb interaction is treated with perturbational theory. The effect of AlAs barriers, leading to stronger confinement below and above the QD and on the top of the QD only, will be discussed.

To the best of our knowledge such a comprehensive approach has not been presented so far for three-dimensional structures. A recent treatment of energy levels in pseudomorphic QD's of different geometry (flat cones with a facet angle of 12° on a wetting layer) (Ref. 6) uses several approximations: identical (fully biaxial) strain in the wetting layer *and* the QD was assumed, and the discontinuity of the mass across the heterojunction was not fully taken into account. The strain distribution in *uncovered* QD's has been simulated numerically in Ref. 7 (InAs/GaAs pyramids with {114} sidewalls), using the valence force field model, and in Ref. 8 (truncated pyramidal-shaped $\text{Ge}_{0.85}\text{Si}_{0.15}$ islands on Si) using finite element analysis.

We will first discuss analytical solutions for pseudomorphic structures of high symmetry, i.e., a slab, a cylinder, and a sphere made of isotropic materials, in order to obtain a *general insight* into the fundamental differences of strain distribution in two-, one-, and zero-dimensional nanostructures. In Sec. III numerical results are derived, taking fully into account the orthotropic elasticity tensor in III-V semiconductors.

II. SIMPLE CASES OF PSEUDOMORPHIC NANOSTRUCTURES

We consider three different elementary structures, the pseudomorphic slab (slb), cylinder (cyl), and sphere (sph) made of isotropic materials, taking into account different elastic constants for the inner and outer (barrier) materials. We derive analytical solutions for the strain distribu-

tion in and around them, clarifying the general characteristics of strain in two-, one-, and zero-dimensional structures. The simplifying assumption of isotropic materials does not precisely describe the case of III-V semiconductors. The general behavior of the strain, however, like decay with large distances, and distribution of the anisotropic part of the strain between inner and outer materials, is weakly affected by the simplification.

In the following, all quantities for the inner material shall be indexed with *in*, and those for the outer (barrier) material with *out*. The stress-strain relations for any orthogonal coordinate system (1,2,3) are given by Eq. (1) for isotropic materials. σ denotes the stress, and ϵ the strain tensor, E is the Young modulus, and ν the Poisson ratio:

$$\epsilon_{ij} = \frac{1}{E} [(1+\nu)\sigma_{ij} - \nu\delta_{ij}\sigma_{nn}] . \quad (1)$$

Important combinations of the strain components are the isotropic part I [Eq. (2a)], and the biaxial part B [Eq. (2b)]. Shear components are zero in all cases considered. The strain energy density U_{tot} can be decomposed into $U_{\text{tot}} = U_s U_d$, where U_s is the energy density of dilatation and U_d the energy density of distortion [Eq. (2c)].⁹ The corresponding volume integrals give the respective strain energies E_{tot} , E_s , and E_d :

$$I = \epsilon_{11} + \epsilon_{22} + \epsilon_{33} , \quad (2a)$$

$$B^2 = (\epsilon_{11} - \epsilon_{22})^2 + (\epsilon_{22} - \epsilon_{33})^2 + (\epsilon_{33} - \epsilon_{11})^2 , \quad (2b)$$

$$U_s = \frac{E}{6(1-2\nu)} I^2 , \quad U_d = \frac{E}{6(1+\nu)} B^2 . \quad (2c)$$

The results simplify when the Young moduli of the inner and outer materials are taken to be identical. For III-V semiconductors, $\nu = \frac{1}{3}$ is a typical value and leads to specifically simple expressions.

A. Pseudomorphic slab

This geometry is the simplest one, and has been treated previously in the literature, e.g., Ref. 1. The slab extends along the x and y directions. The outer material imposes (interface) strains $\epsilon_{xx} = \epsilon_{yy} = \epsilon$ onto the inner material, ϵ being the relative lattice mismatch between inner and outer materials. The slab can freely extend in the z direction, and the Poisson effect leads to

$$\epsilon_{zz}^{\text{in}} = -2\epsilon \frac{\nu}{1-\nu} . \quad (3a)$$

We note that the outer material remains completely unstrained.¹⁰ This is even true for nonisotropic material parameters; however, in this case Eq. (3a) becomes dependent on the interface orientation.¹¹ With Eq. (3a) we obtain

$$I_{\text{slb}}^{\text{in}} = 2\epsilon \frac{1-2\nu}{1-\nu} , \quad B_{\text{slb}}^{\text{in}} = \sqrt{2} |\epsilon| \left[\frac{1+\nu}{1-\nu} \right] , \quad (3b)$$

$$U_{s,\text{slb}}^{\text{in}} = \frac{2}{3} E \epsilon^2 \frac{1-2\nu}{(1-\nu)^2} , \quad U_{d,\text{slb}}^{\text{in}} = \frac{1}{3} E \epsilon^2 \frac{1+\nu}{(1-\nu)^2} . \quad (3c)$$

All corresponding quantities in the barrier are zero.

B. Cylinder

The situation for the pseudomorphic (infinitely long) cylinder is more complex: along the cylinder axis, which extends in the z direction, the inner material is strained due to the lattice mismatch ϵ , and the outer material remains unstrained along this direction (this is also true for anisotropic materials¹¹):

$$\epsilon_{zz}^{\text{in}} = \epsilon , \quad \epsilon_{zz}^{\text{out}} = 0 . \quad (4a)$$

For the plane of the circular cross section we introduce polar coordinates (r, θ) . The radius of the cylinder is r_0 , and the cross-sectional area $A_{\text{cyl}} = \pi r_0^2$. As a next step the problems of a hollow cylinder under inner pressure and a massive cylinder under outer pressure are solved under consideration of the constraints given in Eq. (4a) for the outer and inner materials, respectively. With P being the applied pressure, we find

$$\epsilon_{rr}^{\text{in}} = -\frac{1}{E^{\text{in}}} [1 - \nu^{\text{in}} - 2(\nu^{\text{in}})^2] P - \nu^{\text{in}} \epsilon , \quad \epsilon_{\theta\theta}^{\text{in}} = \epsilon_{rr}^{\text{in}} , \quad (4b)$$

$$\epsilon_{rr}^{\text{out}} = -\frac{1 + \nu^{\text{out}}}{E^{\text{out}}} P \left[\frac{r_0}{r} \right]^2 , \quad \epsilon_{\theta\theta}^{\text{out}} = -\epsilon_{rr}^{\text{out}} . \quad (4c)$$

The inner and outer materials are brought into contact (also known as the *shrink fit*, e.g., Ref. 9). The mismatch in lattice constants of inner and outer materials imposes condition (4d), that the difference of the radial displacements u_r in the inner and outer materials at the interface has to be $\delta = \epsilon r_0$:

$$(u_r^{\text{in}} - u_r^{\text{out}})|_{r=r_0} = \delta = \epsilon r_0 . \quad (4d)$$

From this condition we obtain the magnitude of the contact pressure P :

$$P_{\text{cyl}} = -\epsilon \frac{1 + \nu^{\text{in}}}{\frac{1 + \nu^{\text{out}}}{E^{\text{out}}} + \frac{1 - \nu^{\text{in}} - 2(\nu^{\text{in}})^2}{E^{\text{in}}}} , \quad (4e)$$

$$P'_{\text{cyl}} = -\epsilon \frac{E}{2(1-\nu)} .$$

This is the complete solution of the cylinder problem. The prime denotes the case in which the elastic constants for inner and outer materials are identical, which will be used in the following for the sake of simplicity. Finally, for the strains we find

$$\epsilon_{rr}^{\text{in}} = \epsilon_{\theta\theta}^{\text{in}} = \epsilon \frac{1-3\nu}{2(1-\nu)} , \quad \epsilon_{zz}^{\text{in}} = \epsilon , \quad (4f)$$

$$\epsilon_{rr}^{\text{out}} = -\epsilon_{\theta\theta}^{\text{out}} = \epsilon \frac{1+\nu}{2(1-\nu)} \left[\frac{r_0}{r} \right]^2 , \quad \epsilon_{zz}^{\text{out}} = 0 .$$

Note that if $\nu = \frac{1}{3}$, the in-plane strain in the cylinder vanishes. Now we may write I and B and the energy densities:

$$I_{\text{cyl}}^{\text{in}} = 2\epsilon \frac{1-2\nu}{1-\nu} , \quad B_{\text{cyl}}^{\text{in}} = \frac{1}{\sqrt{2}} |\epsilon| \frac{1+\nu}{1-\nu} , \quad (4g)$$

$$I_{\text{cyl}}^{\text{out}} = 0 , \quad B_{\text{cyl}}^{\text{out}} = |\epsilon| \sqrt{\frac{3}{2}} \frac{1+\nu}{1-\nu} \left[\frac{r_0}{r} \right]^2 ,$$

$$U_{s,cyl}^{in} = \frac{2}{3}E\epsilon^2 \frac{1-2\nu}{(1-\nu)^2}, \quad U_{d,cyl}^{in} = \frac{1}{12}E\epsilon^2 \frac{1+\nu}{(1-\nu)^2}, \quad (4h)$$

$$U_{s,cyl}^{out} = 0, \quad U_{d,cyl}^{out} = \frac{1}{4}E\epsilon^2 \frac{1+\nu}{(1-\nu)^2} \left[\frac{r_0}{r} \right]^4.$$

Integrating the energy density in the outer material over the cross-sectional area gives the energy of distortion $E_{d,cyl}^{out}$ in the barrier:

$$E_{d,cyl}^{out} = \frac{1}{4}E\epsilon^2 \frac{1+\nu}{(1-\nu)^2} A_{cyl}. \quad (4i)$$

C. Sphere

For the pseudomorphic sphere we introduce spherical coordinates (ρ, θ, ϕ) . The radius of the sphere is ρ_0 , the sphere's volume is $V_{sph} = 4\pi/3\rho_0^3$, and the relative lattice mismatch shall again be called ϵ . The problem is solved in a similar manner as for the cylinder. First a hollow outer sphere and a massive inner sphere are treated with inner and outer pressures P , respectively.

$$\epsilon_{\rho\rho}^{in} = -\frac{1-2\nu^{in}}{E^{in}}P = \epsilon_{\theta\theta}^{in} = \epsilon_{\phi\phi}^{in}, \quad (5a)$$

$$\epsilon_{\rho\rho}^{out} = -\frac{1+\nu^{out}}{E^{out}}P \left[\frac{\rho_0}{\rho} \right]^3 = -2\epsilon_{\theta\theta}^{out} = -2\epsilon_{\phi\phi}^{out}.$$

The magnitude of the contact pressure P is obtained from the *shrink fit* condition for the radial displacement u_ρ in the inner and outer materials:

$$(u_\rho^{in} - u_\rho^{out})|_{r=r_0} = \delta = \epsilon\rho_0. \quad (5b)$$

The pressure P depends on the elastic constants of the inner and outer materials:

$$P_{sph} = -\epsilon \frac{1}{\frac{1+\nu^{out}}{2E^{out}} + \frac{1-2\nu^{in}}{E^{in}}}, \quad (5c)$$

$$P'_{sph} = -\epsilon \frac{2E}{3(1-\nu)}.$$

The prime again denotes the case in which the elastic constants in the inner and outer materials are identical. This allows considerable simplifications. The strains are

$$\epsilon_{\rho\rho}^{in} = \frac{2}{3}\epsilon \frac{1-2\nu}{1-\nu} = \epsilon_{\theta\theta}^{in} = \epsilon_{\phi\phi}^{in}, \quad (5d)$$

$$\epsilon_{\rho\rho}^{out} = \frac{2}{3}\epsilon \frac{1+\nu}{1-\nu} \left[\frac{\rho_0}{\rho} \right]^3 = -2\epsilon_{\theta\theta}^{out} = -2\epsilon_{\phi\phi}^{out}.$$

In the case of $\nu = \frac{1}{3}$, we find $\epsilon_{\rho\rho}^{in} = \frac{1}{3}\epsilon$. The isotropic and biaxial parts and the energy densities are given by

$$I_{sph}^{in} = 2\epsilon \frac{1-2\nu}{1-\nu}, \quad B_{sph}^{in} = 0, \quad (5e)$$

$$I_{sph}^{out} = 0, \quad B_{sph}^{out} = \sqrt{2}|\epsilon| \left[\frac{1+\nu}{1-\nu} \left[\frac{\rho_0}{\rho} \right] \right]^3, \quad (5f)$$

$$U_{s,sph}^{in} = \frac{2}{3}E\epsilon^2 \frac{1-2\nu}{(1-\nu)^2}, \quad U_{d,sph}^{in} = 0,$$

$$U_{s,sph}^{out} = 0, \quad U_{d,sph}^{out} = \frac{1}{3}E\epsilon^2 \frac{1+\nu}{(1-\nu)^2} \left[\frac{\rho_0}{\rho} \right]^6.$$

Integrating the energy density of distortion over the entire barrier results in

$$E_{d,sph}^{out} = \frac{1}{3}E\epsilon^2 \frac{1+\nu}{(1-\nu)^2} V_{sph}. \quad (5g)$$

D. Comparison and discussion

Around a slab the barrier is completely unstrained. In the cylindrical geometry the strain of the inner material is constant over the cross-sectional area, while the strain in the barrier decays like r^{-2} . Also for a sphere, the strain in the inner material is constant, and the decay in the barrier follows a ρ^{-3} law. The distribution of the distortion energy between inner and outer materials is fundamentally different for the three geometries, while the total strain energies (inner material plus barrier) of all three structures are identical and are given by

$$E_0 = \frac{E\epsilon^2}{1-\nu}. \quad (6)$$

As depicted in Fig. 1 (for $\nu = \frac{1}{3}$), the energy of dilatation (due to the isotropic part of the strain) $E_s = E_0/3$ is completely stored in the inner material for all three cases. In the case of a slab the energy of distortion (due to the anisotropic component of the strain) is fully stored in the slab. For a cylinder the barrier becomes strained and stores $\frac{3}{4}$ of the energy of distortion. For the spherical geometry the entire energy of distortion resides in the outer material. These results may serve as a guideline to understand the distribution of strain and of strain energy in more complicated geometries.

III. STRAIN DISTRIBUTION FOR PYRAMIDS

Now we consider an InAs pyramid (Fig. 2) on a thin InAs layer within GaAs, as has been observed by us for self-organized quantum dots, grown by molecular-beam epitaxy.⁴ The wetting layer thickness L increases with increasing amount of deposited material. For QD's of base length $b = 12$ nm, L amounts to 1.7 ML. For other dot sizes we scale L linearly with the dot's base length, which realistically reproduces experiments on smaller sized

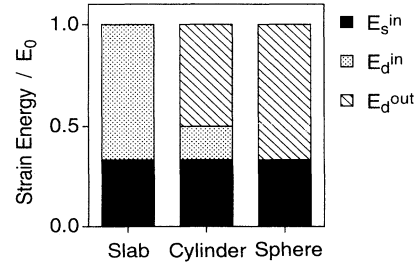


FIG. 1. Energy of dilatation ($E_i = E_i^{in}$, solid black) and energy of distortion in the inner (E_d^{in} , dotted) and outer (E_d^{out} , hatched) materials (with identical elastic constants) for the three different geometries. E_0 is the total strain energy according to Eq. (6a).

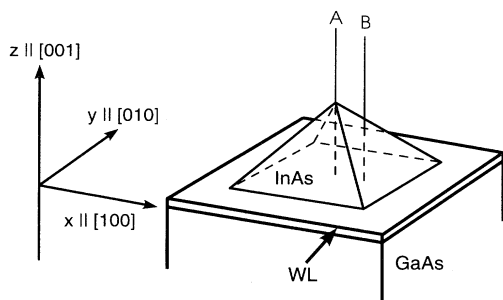


FIG. 2. Schematic drawing of the dot geometry. Lines *A* and *B* denote linescans in [001] direction used below. The origin of the *z* axis is at the lower interface of the wetting layer.

dots.⁴ In order to obtain the three-dimensional strain distribution for this system we perform a numerical simulation in which the total strain energy of the structure in the elastic continuum theory is minimized. This approach is valid down to 1-ML thin films.¹² The equation system was built by finite differences on regular grids, containing about 5×10^5 voxels, using the symmetry of the problem. It was solved by nested iteration, successive over-relaxation Newton iterations. The in-plane boundary conditions for the strain are chosen in agreement with the two-dimensional primitive cubic array of these dots found experimentally.⁴ The typical dot base length is 12 nm, with an interdot distance of 30 nm. However, the strain distribution within the dot depends little on these boundary conditions. We note that the strain distribu-

tion does not depend on the actual *size* of the QD but on its *shape*. All computations, including those for the electronic structure (Sec. IV), have been performed on a DEC Alpha AXP 3000/600 workstation. All material parameters used are given in Table I.

The local variation of strain is visualized in Fig. 3. ϵ_{xx} , ϵ_{yy} , ϵ_{zz} , and ϵ_{xz} are shown in the (010) plane through the top of the pyramid. The main effects can be discussed with linescans along the *z* direction at different positions of the *xy* plane (Fig. 4). The solid line denotes ϵ_{zz} , the dashed line ϵ_{xx} , and the dotted-dashed line ϵ_{yy} in Fig. 4. In Fig. 4(a) the linescan intersecting the wetting layer far from the dot is shown. In Fig. 4(b) the intersection goes through the top of the pyramid (line *A* in Fig. 2). In both cases symmetry imposes $\epsilon_{xx} = \epsilon_{yy}$. In Fig. 4(c) the linescan intersects the dot at one half of the base length in [100] direction from the center (line *B* in Fig. 2). In the wetting layer [Fig. 4(a)] the strain is biaxial and entirely confined to InAs. Compressive (negative) interfacial strain causes an expansion along the *z* direction (ϵ_{zz} is positive), known from quantum wells as tetragonal distortion. The wetting layer is affected by the QD only in its vicinity, within a distance of about half of the pyramid's base length.

Along the linescan through the center of the QD [Fig. 4(b)], a very different situation is revealed. Close to the lower interface, ϵ_{zz} is still positive but much smaller ($\approx 3\%$) than in the wetting layer because the substrate can no longer force the interface lattice constant to be that of GaAs. With increasing height within the dot, ϵ_{zz} changes its sign and becomes negative at the top of the pyramid. This happens because at the very top only

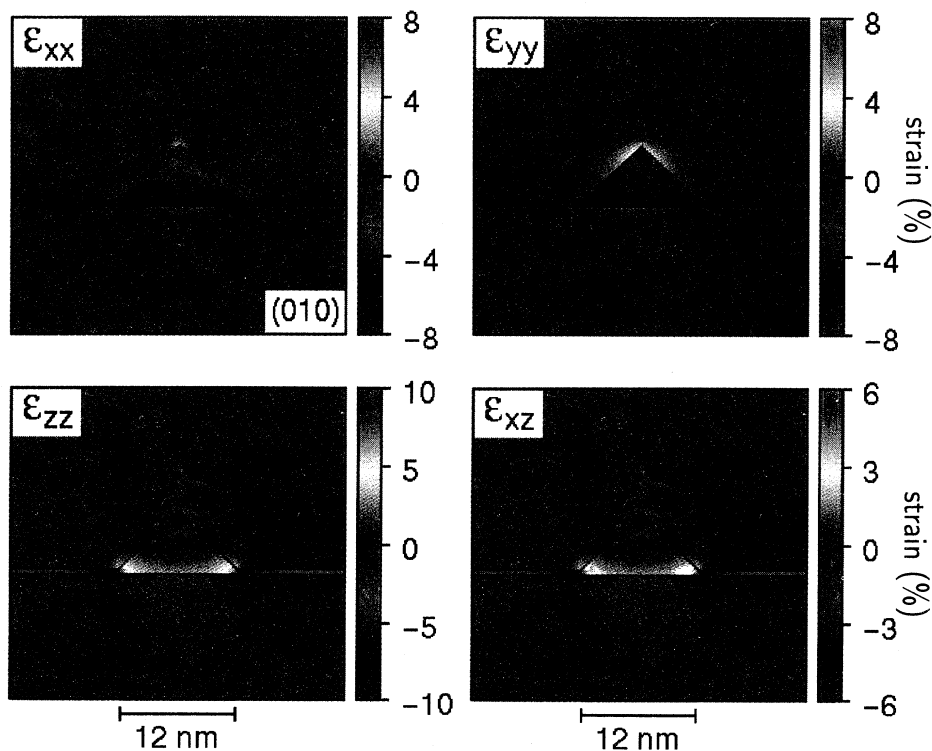


FIG. 3. Strain distribution in the (010) plane through the top of the pyramid.

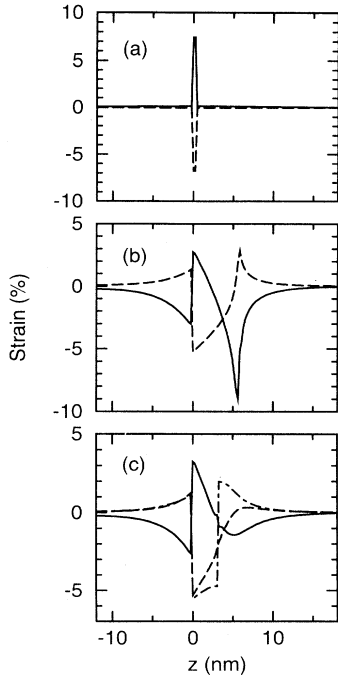


FIG. 4. Strain distribution in and around a pyramidal QD for linescans in the [001] direction: (a) through the wetting layer far away from the dot; and (b) along line *A* and (c) along line *B* of Fig. 2. The solid line denotes ϵ_{zz} , the dashed line ϵ_{xx} , and the dotted-dashed line ϵ_{yy} .

small forces act on the QD in the *xy* plane, but the GaAs barrier compresses the pyramid mainly from the sides along the *z* direction, imposing tensile strain components in the *xy* plane ($\epsilon_{xx} = \epsilon_{yy}$ at the top become positive). Generally, however, the strain is still compressive even at the top of the pyramid ($\text{Tr}\epsilon < 0$). Around the pyramid the barrier also becomes significantly strained ($\approx 3\%$ close to the interfaces).

The character of the strain is not determined by the separate components of the strain tensor, but by decomposing the strain tensor into the isotropic (hydrostatic) and anisotropic parts according to Eqs. (2a) and (2b). Additionally shear strains ϵ_{ij} ($i \neq j$) also exist, which turn out to be significant close to the pyramid edges (intersections of the {011} side facets). In Fig. 5 we compare the linescans through the dot center (line *A* in Fig. 2) of the hydrostatic part *I* and biaxial part *B* of the strain tensor. As expected from the simple considerations in Sec. IID the inner part of the QD contains nearly homogeneous hydrostatic strain, while the barrier exhibits almost no hydrostatic strain. The biaxial strain is transferred to a significant amount into the barrier around the QD and has a distinct minimum in the QD.

We note that the strain distribution presented here may not be directly compared to TEM data if thin foil relaxation plays a significant role. In this case different boundary conditions were required for the calculation.

From the strain distribution we estimate the phonon energy in the QD. While for monolayer InAs/GaAs

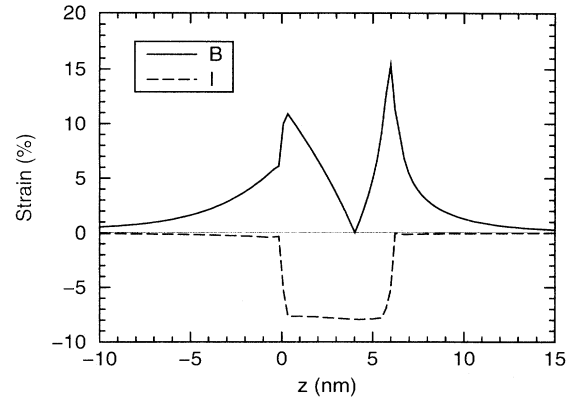


FIG. 5. Hydrostatic (dashed line) and biaxial (solid line) strains in the pyramidal QD along line *A* in Fig. 2.

quantum wells the shift of the phonon energy due to strain is almost compensated by the strong confinement effects,¹³ no significant confinement effects are expected for the fairly large dots. As an approximation we calculate at each point in the InAs the bulk optical-phonon energy for the respective local strain state following Eq. (2) of Ref. 14. In Fig. 6 we show the histogram of the strain-induced relative shifts of the optical-phonon energies. The doublet and singlet components are obvious; the sharp peaks are due to the (more homogeneously strained) wetting layer, and the broader ones to the QD. One of the doublet components becomes the shift of the LO phonon in III-V zinc-blende-type material.¹⁴ With a bulk LO-phonon energy of 29.9 meV, the expected average strain-induced shift of the LO-phonon energy in the QD is $\Delta E = 2.2$ meV, giving $E_{LO}^{QD} = 32.1$ meV. Recent investigations of multiphonon relaxation in QD's of this pyramidal geometry⁵ have yielded an experimental value of $E_{LO}^{QD} = 32.2 \pm 0.5$ meV, in good agreement with our theory. We note that, as long as phonon confinement effects play no role, the phonon energy in the QD is independent of the QD size in the framework presented here.

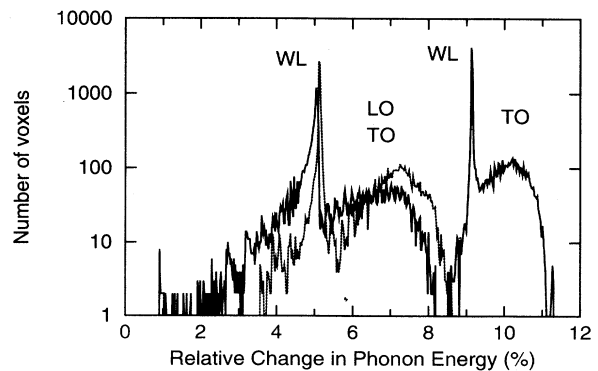


FIG. 6. Histogram of the relative shift of optical-phonon energies in the InAs. Sharp peaks are due to the (more homogeneously strained) wetting layer, broader ones to QD's. One of the doublet components is the strain-induced shift of the LO phonon.

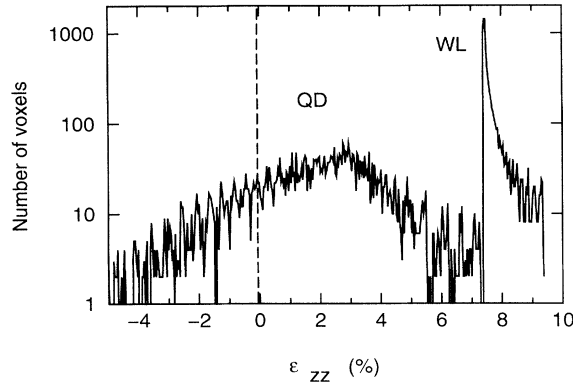


FIG. 7. Histogram of ϵ_{zz} in InAs (wetting layer and QD).

An important figure for x-ray-diffraction experiments is the distribution of strain ϵ_{zz} in the dot, affecting, e.g., the position of the (004) reflection. Figure 7 depicts the histogram of ϵ_{zz} in the InAs. The sharp peak is due to the (more homogeneously strained) wetting layer, and represents the biaxial strain in a quantum well. The broad peak with its maximum at about 3% is due to the QD, and shows that the strain in the z direction is quite inhomogeneous and strongly relaxed. This is important for the future interpretation of x-ray-diffraction data from such nanostructures.

IV. ELECTRONIC STRUCTURE OF PYRAMIDAL QD's

The strain-induced modification of the band gap is obtained from the strain tensor in the following way: We decouple the conduction band from the valence bands and for the strain-induced shift of the conduction band δE_c use Eq. (7), which depends only on the hydrostatic component of the strain:

$$\delta E_c = -a_c(\epsilon_{xx} + \epsilon_{yy} + \epsilon_{zz}). \quad (7)$$

The shift and splitting of the three valence bands are obtained from the 6×6 Hamiltonian H_e for the three valence bands under strain as given in, e.g., Refs. 15 and 16. The top valence band under the present essentially compressive strain is the $|\frac{3}{2}, \pm\frac{3}{2}\rangle$ band (heavy holes). The other two bands are split far from the valence-band edge, and will play no role in the following.

Further refinement could be obtained by taking into account the gradient of the strain tensor as outlined in Ref. 16. For a deduction of the electron and hole confinement potentials, the strain-induced changes have to be added to the heterostructure band offsets. The offset ratio Q_0 for the unstrained bands is taken from the difference in absolute energetic position of the average valence band $E_{v,av}$,¹⁷ and amounts to $Q_0 = 85\%$ for InAs/GaAs. The confinement potentials for electrons and holes will be denoted as $V_e(\mathbf{r}_e)$ and $V_h(\mathbf{r}_h)$, respectively, in the following.

The shear strains induce a piezoelectric polarization \mathbf{P} which creates fixed charges ρ_P ,

$$\rho_P = -\text{div}\mathbf{P}, \quad P_i = e_{ijk}\epsilon_{jk}, \quad (8a)$$

which reside close to the pyramid's edges and have opposite signs for adjacent edges (Fig. 8). Positive charges reside on the outer edges of $\{112\}A$ planes. Since the piezoelectric module $e_{14} = e_{123}$ of InAs is a factor of 4 smaller than that of GaAs, the resulting piezoelectric potential

$$V_P(\mathbf{r}) = \frac{1}{4\pi\epsilon_0\epsilon_r} \iiint \frac{\rho_P(\mathbf{r}')}{|\mathbf{r}-\mathbf{r}'|} d^3\mathbf{r}' \quad (8b)$$

is present mainly in the barrier. In Fig. 8 the isopotential surfaces for $|V_P| = 30$ meV are displayed. The potential V_P has quite a complicated geometry and vanishes along line A of Fig. 2. We note that V_P is not independent of the QD size but scales linearly with the pyramid base length. Inclusion of V_P in the calculations reduces the

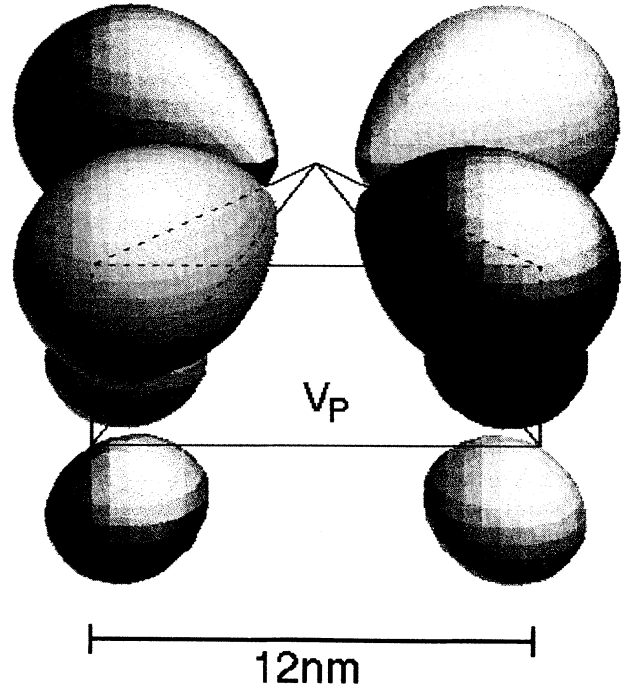
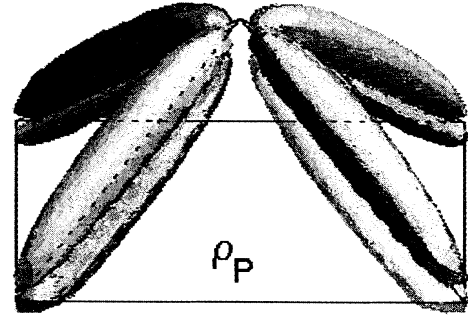


FIG. 8. Upper part: Piezoelectric charge density due to shear strain in a 12-nm QD (isosurfaces for a volume charge density $|q| = 0.3 e \text{ nm}^{-3}$). The front left edge is on a $\{112\}A$ surface; thus the outer charge (red) is positive. Lower part: Resulting piezoelectric potential (isosurface for $|V_P| = 30$ meV). In both parts equal color means equal sign.

TABLE I. Material properties of GaAs and InAs used in the calculations. Symbols are explained in the text; K_{ij} are phonon deformation potentials as used in Ref. 14.

Property	a_0 (nm)	C_{11} (10^{10} Pa)	C_{12} (10^{10} Pa)	C_{44} (10^{10} Pa)			
GaAs	0.565 33	12.2	5.5	6.0			
InAs	0.605 84	8.3	4.5	4.0			
Property	$E_{v,av}$ (eV)	Δ_0 (eV)	E_{gap} (eV)	a (eV)	a_c (eV)	b (eV)	d (eV)
GaAs	-6.92	0.34	1.519	-8.33	-7.17	-1.6	-4.23
InAs	-6.67	0.38	0.41	-6.08	-5.08	-1.8	-3.1
Property	e_{14} (Cm^{-2})	m_e (m_0)	$m_{\text{hh},z}$ (m_0)	$m_{\text{hh},xy}$ (m_0)		ϵ_r	
GaAs	0.16	0.0665	0.0377	0.112		12.5	
InAs	0.045	0.023	0.0341	0.035		15.2	
Property	$K_{11} + 2K_{12}$		$K_{11} - K_{12}$		K_{44}		
GaAs	-7.4		0.7		-0.53		
InAs	-6.4		0.57		-0.76		

symmetry of the QD z axis from C_{4v} to C_{2v} , and thus leads to a lifting of degeneracies. For nondegenerated levels, corrections in first-order perturbation theory are zero. Since the energies of levels involved in optical transitions are generally affected by less than 1 meV, V_p will be neglected for the main part of the paper. It will be discussed in detail in Sec. IV D.

The Hamiltonian H for an electron-hole pair in the QD is given by

$$H(\mathbf{r}_e, \mathbf{r}_h) = H_{e,\text{kin}}(\mathbf{r}_e) + V_e(\mathbf{r}_e) + H_{h,\text{kin}}(\mathbf{r}_h) + V_h(\mathbf{r}_h) + H_c(\mathbf{r}_e, \mathbf{r}_h), \quad (9a)$$

$$H_{e,\text{kin}}(\mathbf{r}_e) = \frac{\hbar^2}{2} \sum_{i=x,y,z} \nabla_i \frac{1}{m_e(\mathbf{r}_e)} \nabla_i, \quad (9b)$$

$$H_{h,\text{kin}}(\mathbf{r}_h) = \frac{\hbar^2}{2} \left[\sum_{i=x,y} \nabla_i \frac{1}{m_{h,\parallel}(\mathbf{r}_h)} \nabla_i + \nabla_z \frac{1}{m_{h,\perp}(\mathbf{r}_h)} \nabla_z \right], \quad (9c)$$

$$H_c(\mathbf{r}_e, \mathbf{r}_h) = \frac{-e^2}{4\pi\epsilon_r\epsilon_0} \frac{1}{|\mathbf{r}_e - \mathbf{r}_h|}. \quad (9d)$$

The Coulomb interaction H_c is the only term which depends on coordinates of both electrons and holes, and couples their motion. Since the QD's under consideration are in the *strong confinement regime*,¹⁸ i.e., their effective radius $r = b / (8\pi)^{1/3} \approx 4$ nm, b being the pyramid base length, is small compared to the bulk exciton Bohr radius ($a_{0,\text{InAs}} = 50$ nm), the size quantization represents the dominating part of the carrier energy. The Coulomb interaction, however, should not be completely neglected. It will be treated as a perturbation of the kinetic eigenstates¹⁹ as outlined below.

First we solve the three-dimensional single-particle effective-mass Schrödinger equation with locally varying, anisotropic effective masses in the confinement potentials. The equation is discretized on an isotropic cubic cell grid

with about 1×10^6 voxels (lateral resolution ≈ 0.5 nm) by applying a symmetrical second-order nonstandard discretization to $(\partial/\partial v)(1/m^*)(\partial/\partial v)$ (harmonic differences²⁰), employing Dirichlet and Neumann boundary conditions. The resulting matrix eigenvalue problem is solved by a nested iteration generalized block Davidson algorithm²¹ with multidirectional tridiagonal preconditioning. Material parameters used are listed in Tables I and II.

In the following we will present calculations for three different material combinations. First we treat InAs QD's in GaAs, a system investigated in detail experimentally. Next we consider AlAs barriers; in this system the quantized InAs electron level lies above the GaAs conduction band for certain QD sizes, making a resonant tunneling diode look feasible. The third system investigated has asymmetric barriers: InAs QD's on GaAs with an upper barrier of AlAs. For this combination wetting layer states are unbound, while QD states are still localized. Carrier relaxation in this system should be quite different from the case of a GaAs top barrier. In Sec. IV D, we outline the effects of the piezoelectric potential for the case of InAs/GaAs QD's.

A. InAs/GaAs

Self-organized InAs/GaAs quantum pyramids form during molecular-beam epitaxy (MBE). The confinement potentials for electrons and holes are shown in Fig. 9 according to the actual sample structure from Ref. 4. The QD's are embedded in a 14-nm GaAs quantum well,

TABLE II. Material properties of $\text{Al}_{0.3}\text{Ga}_{0.7}\text{As}$ and AlAs used in the calculations.

Property	E_{gap} (eV)	m_e (m_0)	$m_{\text{hh},z}$ (m_0)	$m_{\text{hh},xy}$ (m_0)
$\text{Al}_{0.3}\text{Ga}_{0.7}\text{As}$	1.90	0.084	0.409	0.135
AlAs	3.13	0.124	0.51	0.26

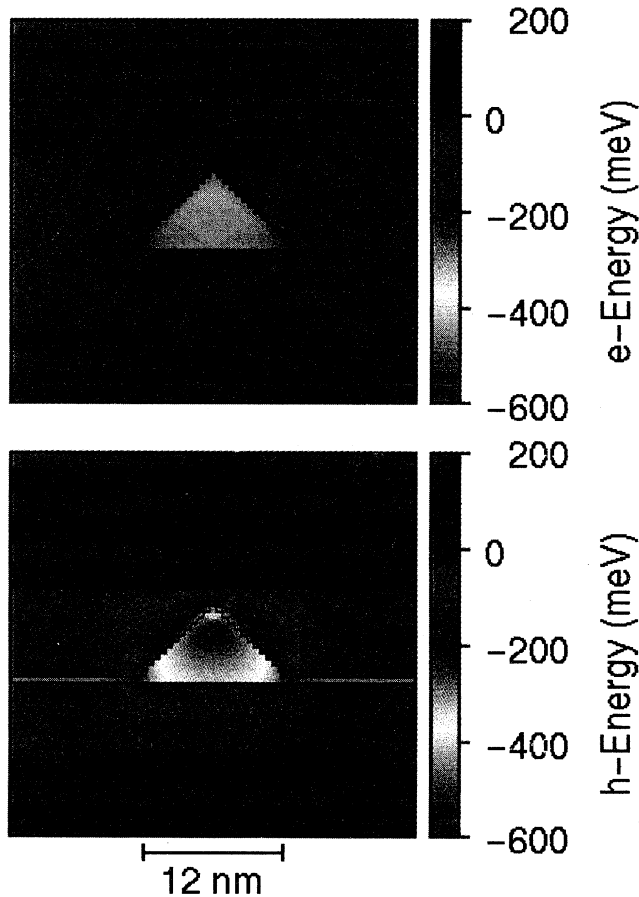


FIG. 9. InAs QD's in GaAs and $\text{Al}_{0.3}\text{Ga}_{0.7}\text{As}$ superlattices. Confinement potential for electrons (top) and holes (bottom), including modification of the band structure due to strain.

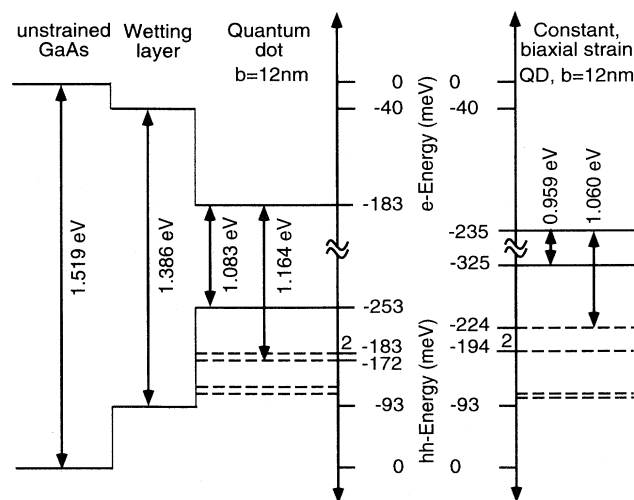


FIG. 10. Electronic levels for an InAs pyramidal QD (12-nm base length) in GaAs with a 1.7-ML wetting layer. Reference levels (origin of electron and hole energy) are bands for unstrained GaAs. On the right side, energy levels are shown for constant biaxial strain.

which itself lies within an $\text{Al}_{0.3}\text{Ga}_{0.7}\text{As}/\text{GaAs}$ (2 nm, 2 nm) superlattice. Inclusion of this superlattice into the confinement potentials (Fig. 9) has been found to effect level energies by less than 0.5 meV compared to pure GaAs barriers for the QD sizes investigated here ($b \geq 6$ nm). All further results in this section have been obtained with pure GaAs barriers.

In the following we will first treat the single-particle problems for electrons and holes, and then consider their Coulomb correlation. For the typical InAs QD sizes developing in epitaxy, there exists only one bound electron level. Higher levels hybridize with the wetting layer. Figure 10 depicts the term scheme for QD's and WL's: the zeroes of the electron and hole energy scales are taken at the unstrained GaAs conduction and valence bands, respectively. In Fig. 11 the electron (ground state) wave function in the QD is shown in a perspective view and in a (010) or (100) cross section. The isosurface containing 70% of the wave-function probability lays almost completely within the dot. The heavy-hole ground-state wave function is shown in Fig. 12 together with excited-state wave functions having energies below the wetting layer. Due to the strain-induced potential the hole ground state is squeezed at the bottom of the QD. The excited states are classified according to their nodes in x , y , and z directions. Their energy levels can be found in Fig. 10, where the hole's energy scale starts at the valence band of unstrained GaAs. The first excited level ($E = -183$ meV) is twofold degenerate with states $|100\rangle$ and $|010\rangle$. They can be rotated in their two-dimensional subspace, giving, e.g., the wave functions shown in the second row of Fig. 12. Those wave functions, located in the second row of Fig. 12, will develop into eigenstates when the piezoelectric potential is included (see the lower part of Fig. 12, and the discussion in Sec. IV D). With increasing energy the wave function increasingly leaks into the wetting layer.

The variation of electron and hole levels with varying quantum dot size is shown in Fig. 13. Only one electron

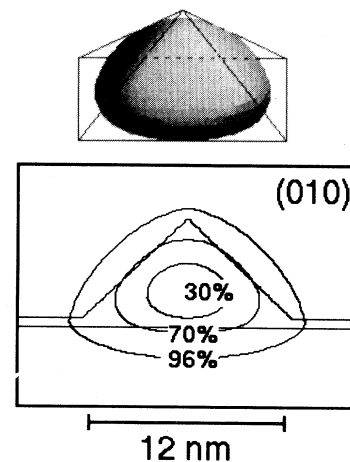


FIG. 11. Three-dimensional view of the isosurface (the probability of finding the electron inside is 70%), and cross section with isolines (30%, 70%, and 96% probabilities of finding the electron inside) of the squared electron ground-state wave function for a $b = 12$ -nm InAs QD. The cross section is a (100) or (010) plane through the dot center.

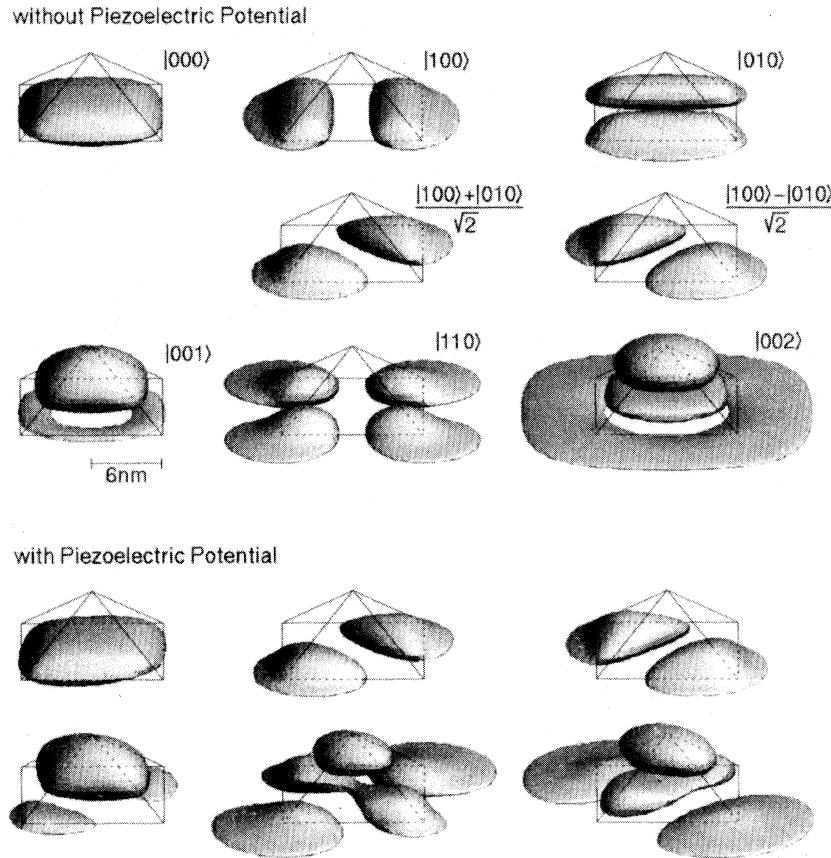


FIG. 12. Three-dimensional view of the isosurface of the squared heavy-hole wave functions (the probability of finding the hole inside is 70%) for $b=12$ nm QD. The upper part is calculated without inclusion of the piezoelectric potential. The levels are classified by their knots in x , y , and z directions; their energies are given in Fig. 10. The lower part is calculated with the inclusion of the piezoelectric potential from Fig. 8. Degeneracy of former $|100\rangle$ and $|010\rangle$ levels is lifted (for splitting, see Fig. 20).

level exists, whose energy rises strongly until for about $b < 6$ nm no bound-electron state exists anymore. Several hole levels are found (wave functions for $b=12$ nm were shown in Fig. 12); the topmost merge one after the other with the wetting layer for decreasing dot size. For electrons a spherical approximation of the pyramid already gives satisfactory energies, since the strain-induced band-gap modulation within the dot is quite homogeneous and the mass is isotropic. However, for different confinement strengths (e.g., for AlAs barriers; see Sec. IV C) the spherical approximation gives poor results. For a given pyramid base length b we consider a sphere of radius r having the same volume. The electron confinement potential is taken as $V_0 = -450$ meV, the average over the QD. The ground-state energy for electrons is obtained from the equation given in Ref. 22, taking the mass discontinuity into account. It is shown as dashed line for electrons in Fig. 13. For all dot sizes the spherical approximation yields electron energies close to those calculated using the exact treatment. For holes the spherical approximation cannot be applied. The adiabatic approximation, i.e., solving the one-dimensional Schrödinger equation in the z direction and subsequently solving a two-dimensional in-plane Schrödinger equation, has been found to work poorly for both electrons and holes. Assuming the strain distribution as a constant (biaxial) strain in the InAs (the same strain in the WL and QD) results in a very poor approximation for our pyramid-

ids: The ground-state energies are wrong by more than 50 meV for both electrons and holes, the order of excited hole states is changed, and the hole sublevel separation is wrong by up to 100%. The schematic level scheme is shown on the right side of Fig. 10.

Despite the difference in the shape of the wave function, the wave-function overlap of the electron and hole ground states is 88% for the $b=12$ -nm QD. However, there is a fairly large local charge non-neutrality, causing a dipole moment. In Fig. 14 we depict the local charge density $q_{\text{local}} = \rho_e + \rho_{\text{hh}}$ of the ground state (isosurface for $|q_{\text{local}}| = 0.2\rho_{e,\text{max}}$), which has a dipole moment $p = \int \rho(\mathbf{x}') \mathbf{x}' d^3\mathbf{x}'$ of $|p| = 0.77 e \text{ nm} = 1.2 \times 10^{-31} \text{ C m}$. This dipole moment might play an important role for QD interaction with light and optical phonons. Due to in-plane symmetry the overlap between the $|100\rangle$ and $|010\rangle$ hole states with the electron ground state is zero. But the overlap of the electron with the $|001\rangle$ hole state is finite and amounts to 34% for $b=12$ nm. We believe we have observed this transition in absorption^{4,23} and in luminescence at higher excitation.²³

With respect to energy relaxation in the QD's a detailed look at the hole levels (Fig. 15) is very interesting. For typical dot sizes the $|100\rangle$, $|001\rangle$, and $|110\rangle$ levels are close to two, three, and four LO-phonon energies (dashed lines in Fig. 15), respectively, separated from the hole ground state, taken as zero energy. Thus multiphonon relaxation processes of excited holes into the hole

ground state are energetically possible. Such multiphonon (or multiple single phonon) relaxation processes probed by excitation spectroscopy have been reported by Heitz *et al.*⁵

So far only single-particle eigenstates of the kinetic energy have been considered. The Coulomb interaction can be treated with standard perturbation theory. If $|0\rangle$ and E_0 are the unperturbed ground-state vector and energy,

$$\begin{aligned} \langle 00|H_{\text{Coulomb}}|\alpha\beta\rangle &= -V_{\alpha\beta} \\ &= -\int d^3\mathbf{r}_e \int d^3\mathbf{r}_h \Psi_0(\mathbf{r}_e)\Psi_0(\mathbf{r}_h) \frac{e^2}{4\pi\epsilon_0\epsilon_r} \frac{1}{|\mathbf{r}_e - \mathbf{r}_h|} \Psi_\alpha(\mathbf{r}_e)\Psi_\beta(\mathbf{r}_h). \end{aligned} \quad (10b)$$

Since there is only one bound electron state, we have to consider only excited hole states in the second order of the perturbation. It turns out that V_{00} represents the dominating term, and second-order corrections are at least two orders of magnitude smaller and therefore negligible. This *a posteriori* justifies our perturbational approach. The exciton binding energy E_X obtained this way is depicted in Fig. 16 as a function of pyramid size. For $b = 12$ nm we find $E_X = 20$ meV. Compared to the bulk exciton binding energy of InAs of 1 meV, it is drastically enhanced. We note that we have used $\epsilon_r = 15.2$

the correction ΔE due to a perturbational Hamiltonian H' is given to second order as

$$\Delta E = \langle 0|H'|0\rangle + \sum_{\alpha} \frac{|\langle 0|H'|\alpha\rangle|^2}{E_{\alpha} - E_0}. \quad (10a)$$

α sums over excited states. In our case the matrix elements for the one-particle electron and hole kinetic eigenstates α, β are

$= \epsilon_{r, \text{InAs}}$ throughout the calculation, thus neglecting image charge effects due to the different static dielectric constants in the QD and the barrier. Since the dielectric constant is smaller in the barrier, the true exciton binding energy will be slightly larger.²⁴

Now we have a satisfactory solution of our Hamiltonian Eq. (9a). The resulting optical transition energies (including the exciton binding energy) are shown in Fig. 17 for recombination of electrons with holes in their ground state and the $|001\rangle$ state.

B. InAs/AlAs

Since the elastic properties and the lattice constant of AlAs are very similar to GaAs, we use the same strain distribution as for the InAs/GaAs case. The confinement potentials are only modified due to the higher band gap of AlAs. For the calculation we use the Γ gap contributing an additional conduction- (valence-) band offset of 1079 meV (532 meV). The AlAs/InAs QD's are of in-

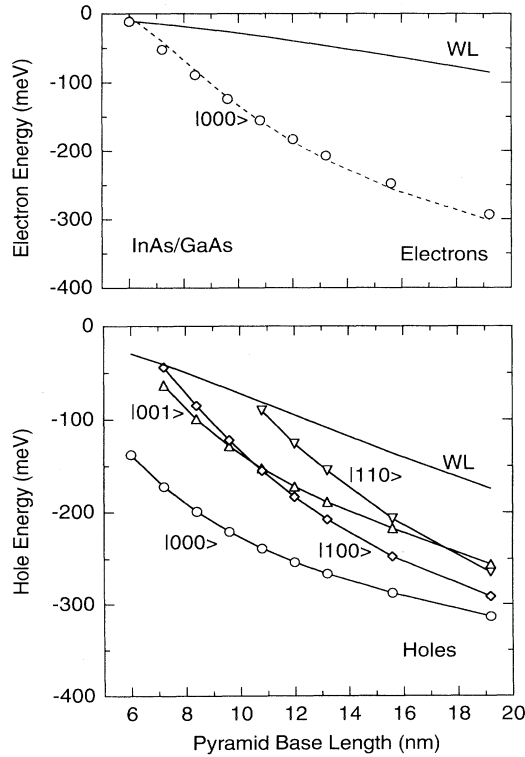


FIG. 13. Variation of electron and heavy-hole levels as a function of QD size. The dashed line for electrons is obtained from the spherical approximation, with the confinement potential averaged over the dot.

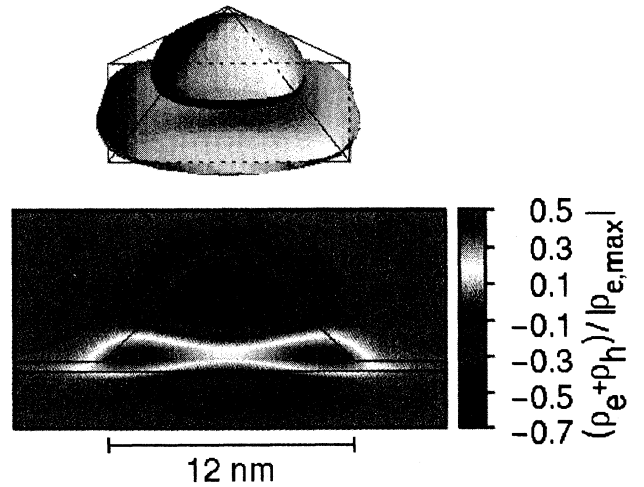


FIG. 14. Local charge density $q_{\text{local}} = \rho_e + \rho_{\text{hh}}$ as an isosurface for $|q_{\text{local}}| = 0.2\rho_{e,\text{max}}$ in a 12-nm base length pyramidal quantum dot. The lower cloud is positively charged, the upper cloud negatively. The dipole moment of this charge distribution is 0.77 e nm.

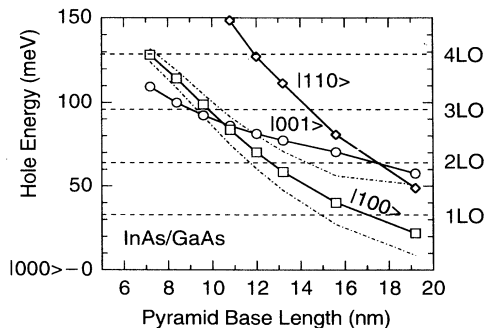


FIG. 15. Hole subband energies with respect to the dot ground-state structure as a function of dot size. Horizontal dashed lines are separated integer multiples of the dot LO-phonon energy of 32.2 meV. Dash-dotted lines show the inclusion of the piezoelectric potential (see Sec. IV D and Fig. 20).

terest for resonant tunneling structures if the QD electron ground state is so strongly confined that it lies above the GaAs (substrate) conduction band. As one can see from Fig. 18 (triangles), this is indeed the case for $b < 11$ nm. In Fig. 18 we include the result for GaAs barriers (Fig. 13) as circles for comparison. As we pointed out above, the spherical approximation in this case works poorly, and yields energies about 70–30 meV (for $b = 6$ –20 nm) too small.

C. GaAs/InAs/AlAs

This material system with asymmetric barriers is of interest from a fundamental point of view. Due to the asymmetric potential well the WL ground state lies above the level for unstrained GaAs for electrons and holes, and is no longer bound. The QD ground state, however, remains localized, i.e., the quantized electron level lies below the GaAs conduction band, for $b \geq 9$ nm (squares in Fig. 18). Due to the heavier mass the holes are confined for all QD sizes considered ($b \geq 6$ nm). In Fig. 19 the electron wave function is shown for $b = 12$ nm and asymmetric barriers. The electron is pushed away from the top barrier and penetrates somewhat more into the lower barrier in comparison with Fig. 11 (GaAs as upper barrier).

By comparing experiments on InAs QD structures,

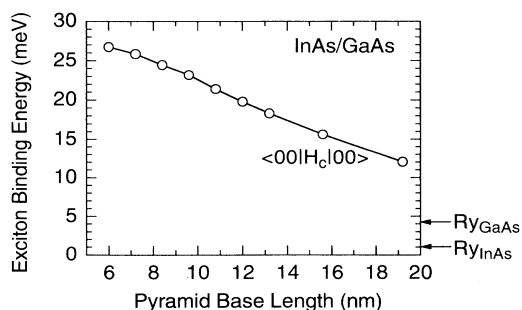


FIG. 16. Exciton binding energy for InAs/GaAs QD's as a function of the pyramid base length.

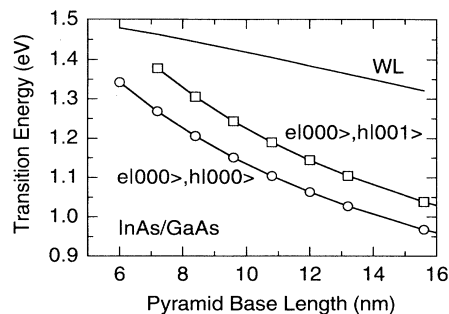


FIG. 17. Transition energy between the electron QD ground state and the hole ground state $|hh_{000}\rangle$ and third excited state $|hh_{001}\rangle$, respectively, as a function of dot size, including the exciton binding energy.

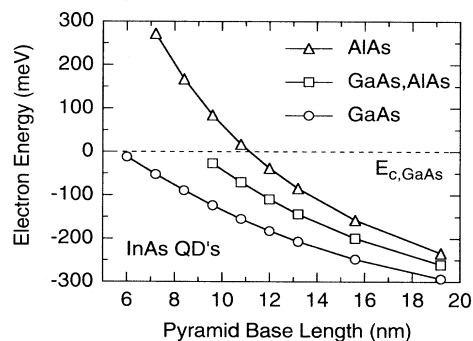


FIG. 18. Electron level in InAs QD's as a function of QD size with respect to the unstrained GaAs conduction band (horizontal dashed line). GaAs barriers (circles), AlAs barriers (triangles), and asymmetric barriers (squares), with GaAs as the lower barrier and AlAs as the upper barrier.

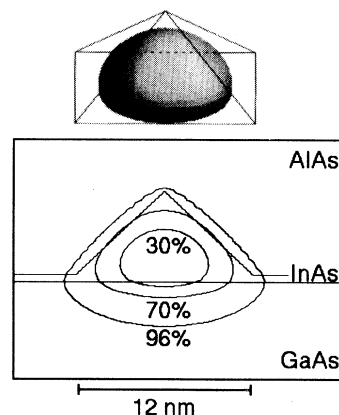


FIG. 19. Three-dimensional view of the isosurface (the probability of finding the electron inside is 70%) and cross section with isolines (30%, 70%, and 96% probabilities of finding the electron inside) of the squared electron ground-state wave function for a $b = 12$ -nm InAs QD between asymmetric GaAs and AlAs barriers. The wave function for the QD in GaAs only is shown in Fig. 10.

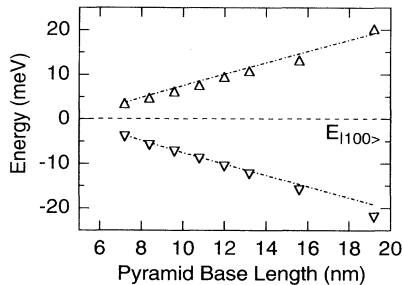


FIG. 20. Energy position relative to the hole ground state for $|100\rangle$ and $|010\rangle$ levels when the piezoelectric potential is neglected ($E_{|100\rangle}$ from Fig. 13, dashed line) and included (triangles). Dash-dotted lines are level positions in first-order perturbation theory for V_p .

grown on the same GaAs substrate and buffer layers, but with different upper barriers (GaAs and AlAs), the role of the wetting layer for carrier capture and relaxation could be identified and separated from that of the GaAs barrier.

D. Impact of piezoelectric potential

In Fig. 8 we showed the piezoelectric charge ρ_p and potential V_p for an InAs/GaAs QD. The maximum of V_p in the clouds is 60 meV. Due to the lack of inversion symmetry of V_p with respect to the $[100]$ and $[010]$ directions, the symmetry of the pyramid z axis is lowered from C_{4v} to C_{2v} . In Fig. 12 we compare the hole wave functions for calculations with and without V_p . The electron wave function is very weakly distorted and cannot be distinguished from that shown in Fig. 11. The $|100\rangle$ and $|010\rangle$ hole levels were degenerate because the Hamiltonian was invariant under 90° rotation (operation C_4) around the z axis through the dot center. Inclusion of the piezoelectric potential now removes that symmetry and lifts the degeneracy. The splitting of both levels, obtained from the full numerical calculation including V_p , is compiled in Fig. 20 as triangles. The lower- (higher-) energy hole level is located in the $\{111\}A$ ($\{111\}B$) corners of the pyramid because there the charge residing on the inner side of the edge is negative (positive), respectively. The dash-dotted lines in Fig. 20 are the level shifts in first-order perturbation theory for V_p . First-order corrections for nondegenerate levels are zero. Second-

order perturbation theory yields small corrections (< 1 meV) for $b \leq 14$ nm practically only for the $|000\rangle$ and $|002\rangle$ states. However, for larger structures and QD materials with larger piezoelectric moduli, V_p makes significant contribution and thus should generally be taken into consideration.

V. CONCLUSION

We have calculated the strain distribution in and around InAs/GaAs quantum dots of pyramidal shape on a thin wetting layer. Such QD's have been observed in TEM analysis of MBE-grown structures. The hydrostatic part of the strain is mainly confined within the dot. The anisotropic part is shared between the dot and the surrounding barrier, and has a minimum in the dot. The estimated strain-induced shift of LO-phonon energy agrees with our experimental data. Additionally the TO-phonon energies in the QD are determined.

From the strain the modification of conduction and valence bands is obtained. With our general purpose program to solve a three-dimensional effective-mass Schrödinger equation with arbitrarily varying potential and anisotropic mass, we obtain the eigenenergies and wave functions. The QD energy levels and hole sublevel structure agree with recent luminescence and absorption data for such dots. For typical dot sizes investigated here (pyramid base length $b=6-20$ nm) only one confined electron state exists. Ground-state wave functions of electrons and heavy holes have a large overlap ($\approx 90\%$); however, a quite large local charge non-neutrality remains. Excited hole level wave functions are classified by their nodes in x , y , and z directions. The exciton binding energy can be calculated in first-order perturbation theory, and typically amounts to 20 meV. Piezoelectric effects lift degeneracies and distort the hole wave functions, but affect the energies of allowed optical transitions rather weakly. InAs QD's with AlAs barriers and asymmetric AlAs and GaAs barriers are also treated.

ACKNOWLEDGMENTS

We are indebted to N. N. Ledentsov, R. Heitz, and V. Türk for valuable discussions and support. F. Heinrichsdorff stimulated the investigation of the asymmetric barrier structure. This work was funded by the Deutsche Forschungsgemeinschaft in the framework of Sfb 296.

*Electronic address: mariusgr@w422zrz.physik.tu-berlin.de

WWW-server at <http://sol.physik.tu-berlin.de/>

¹G. C. Osbourne, Phys. Rev. B **27**, 5126 (1983).

²E. Yablonovitch and E. O. Kane, J. Lightwave Technol. **9**, 991 (1988).

³V. A. Shchukin, N. N. Ledentsov, M. Grundmann, P. S. Kop'ev, and D. Bimberg (unpublished).

⁴M. Grundmann, J. Christen, N. N. Ledentsov, J. Böhrer, D. Bimberg, S. S. Ruvimov, P. Werner, U. Richter, U. Gösele, J. Heydenreich, V. M. Ustinov, A. Yu. Egorov, A. E. Zhukov, P. S. Kop'ev, and Zh. I. Alferov, Phys. Rev. Lett. **74**, 4043 (1995); M. Grundmann, N. N. Ledentsov, R. Heitz, L. Eckey,

J. Christen, J. Böhrer, D. Bimberg, S. S. Ruvimov, P. Werner, U. Richter, J. Heydenreich, V. M. Ustinov, A. Yu. Egorov, A. E. Zhukov, P. S. Kop'ev, and Zh. I. Alferov, Phys. Status Solidi B **188**, 249 (1995); N. N. Ledentsov, M. Grundmann, N. Kirstaedter, J. Christen, R. Heitz, J. Böhrer, F. Heinrichsdorff, D. Bimberg, S. S. Ruvimov, P. Werner, U. Richter, U. Gösele, J. Heydenreich, V. M. Ustinov, A. Yu. Egorov, M. V. Maximov, P. S. Kop'ev, and Zh. I. Alferov, in *Proceedings of the 22nd International Conference on Semiconductors, Vancouver, Canada*, edited by D. J. Lockwood (World Scientific, Singapore, 1995), Vol. 3, p. 1855; S. Ruvimov, P. Werner, K. Scheerschmidt, J. Heydenreich, U.

- Richter, N. N. Ledentsov, M. Grundmann, D. Bimberg, V. M. Ustinov, A. Yu. Egorov, P. S. Kop'ev, and Zh. I. Alferov, *Phys. Rev. B* **51**, 14 766 (1995).
- ⁵R. Heitz, N. N. Ledentsov, M. Grundmann, L. Eckey, D. Bimberg, V. M. Ustinov, A. Yu. Egorov, A. E. Zhukov, P. S. Kop'ev, M. V. Maximov, and Zh. I. Alferov, *Surf. Sci.* (to be published).
- ⁶J.-Y. Marzin and G. Bastard, *Solid State Commun.* **92**, 437 (1994).
- ⁷C. Priester, I. Lefebvre, G. Allan, and M. Lannoo, in *Mechanisms of Thin Film Evolution*, edited by S. M. Yalisove, C. V. Thompson, and D. J. Eaglesham, MRS Symposia Proceedings No. 317 (Materials Research Society, Pittsburgh, 1994), p. 131.
- ⁸S. Christiansen, M. Albrecht, H. P. Strunk, and H. J. Maier, *Appl. Phys. Lett.* **64**, 3617 (1994).
- ⁹A. S. Saada, *Elasticity Theory and Applications* (Pergamon, New York, 1974).
- ¹⁰This is exactly true only in the limit of an infinitely thick substrate. For finite substrate thickness, substrate bending occurs, which can be neglected in our treatment, since the substrate thickness is much larger than the thickness of the strained material.
- ¹¹M. Grundmann, O. Stier, and D. Bimberg, *Phys. Rev. B* **50**, 14 187 (1994).
- ¹²J. Bernard and A. Zunger, *Appl. Phys. Lett.* **65**, 165 (1994).
- ¹³P. D. Wang, N. N. Ledentsov, C. M. Sotomayor Torres, I. N. Yassievich, A. Pakhomov, A. Yu. Egorov, A. E. Zhukov, P. S. Kop'ev, and V. M. Ustinov, *Phys. Rev. B* **50**, 1604 (1994).
- ¹⁴F. Cerdeira, C. J. Buchenauer, F. H. Pollak, and M. Cardona, *Phys. Rev. B* **5**, 580 (1972); B. Jusserand and M. Cardona, *Light Scattering in Solids V: Superlattices and Other Microstructures*, Topics in Applied Physics Vol. 66 (Springer, Berlin, 1989), p. 49.
- ¹⁵F. H. Pollak, *Semicond. Semimetals* **32**, 17 (1990).
- ¹⁶Y. Zhang, *Phys. Rev. B* **49**, 14 352 (1994).
- ¹⁷Ch. G. Van der Walle, *Phys. Rev. B* **39**, 1871 (1989).
- ¹⁸A. L. Efros and A. L. Efros, *Fiz. Tech. Poluprovodn.* **16**, 1209 (1981) [*Sov. Phys. Semicond.* **16**, 772 (1982)].
- ¹⁹L. Bányai, *Phys. Rev. B* **39**, 8022 (1989).
- ²⁰T. S. Li and K. J. Kuhn, *J. Comput. Phys.* **110**, 292 (1994).
- ²¹C. W. Murray, S. C. Racine, and E. R. Davidson, *J. Comput. Phys.* **103**, 382 (1992).
- ²²D. B. Tran Thoai, Y. Z. Hu, and S. W. Koch, *Phys. Rev. B* **42**, 11 261 (1990).
- ²³M. Grundmann, *Adv. Solid State Phys.* (to be published).
- ²⁴D. B. Tran Thoai, R. Zimmermann, M. Grundmann, and D. Bimberg, *Phys. Rev. B* **42**, 5906 (1990).

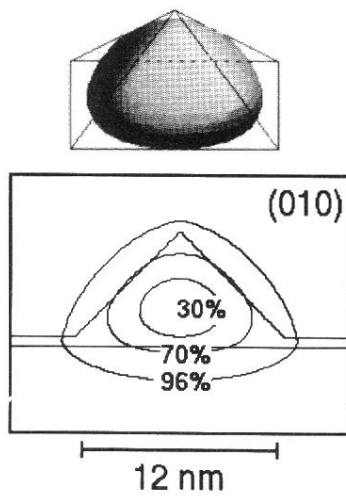
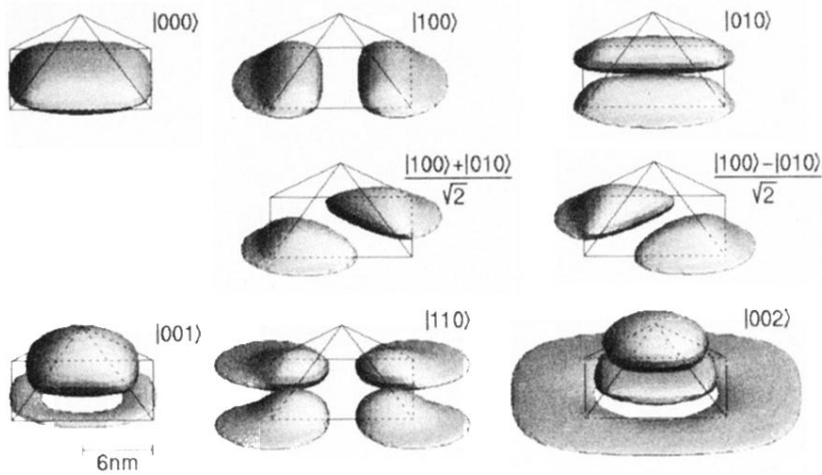


FIG. 11. Three-dimensional view of the isosurface (the probability of finding the electron inside is 70%), and cross section with isolines (30%, 70%, and 96% probabilities of finding the electron inside) of the squared electron ground-state wave function for a $b = 12$ -nm InAs QD. The cross section is a (100) or (010) plane through the dot center.

without Piezoelectric Potential



with Piezoelectric Potential

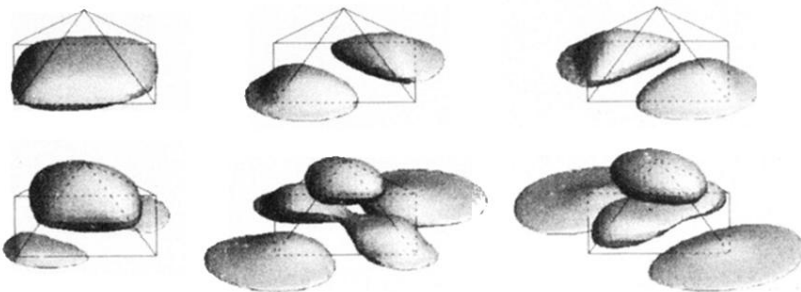


FIG. 12. Three-dimensional view of the iso-surface of the squared heavy-hole wave functions (the probability of finding the hole inside is 70%) for $b = 12$ nm QD. The upper part is calculated without inclusion of the piezoelectric potential. The levels are classified by their knots in x , y , and z directions; their energies are given in Fig. 10. The lower part is calculated with the inclusion of the piezoelectric potential from Fig. 8. Degeneracy of former $|100\rangle$ and $|010\rangle$ levels is lifted (for splitting, see Fig. 20).

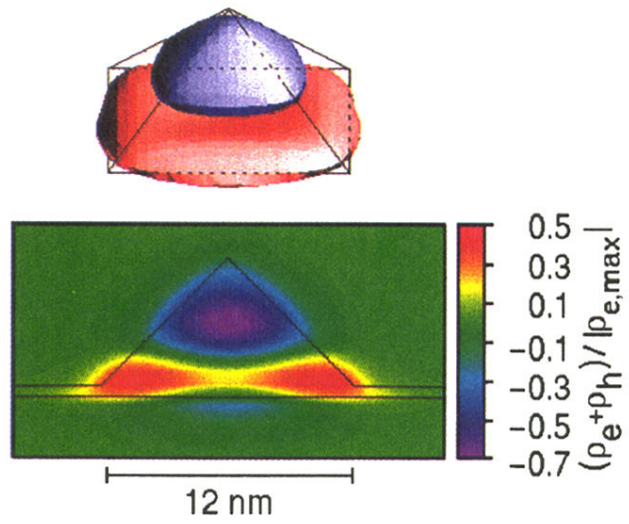


FIG. 14. Local charge density $q_{\text{local}} = \rho_e + \rho_{\text{hh}}$ as an isosurface for $|q_{\text{local}}| = 0.2\rho_{e,\max}$ in a 12-nm base length pyramidal quantum dot. The lower cloud is positively charged, the upper cloud negatively. The dipole moment of this charge distribution is $0.77 e \text{ nm}$.

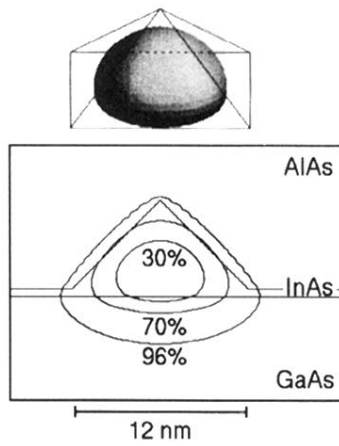


FIG. 19. Three-dimensional view of the isosurface (the probability of finding the electron inside is 70%) and cross section with isolines (30%, 70%, and 96% probabilities of finding the electron inside) of the squared electron ground-state wave function for a $b = 12$ -nm InAs QD between asymmetric GaAs and AlAs barriers. The wave function for the QD in GaAs only is shown in Fig. 10.

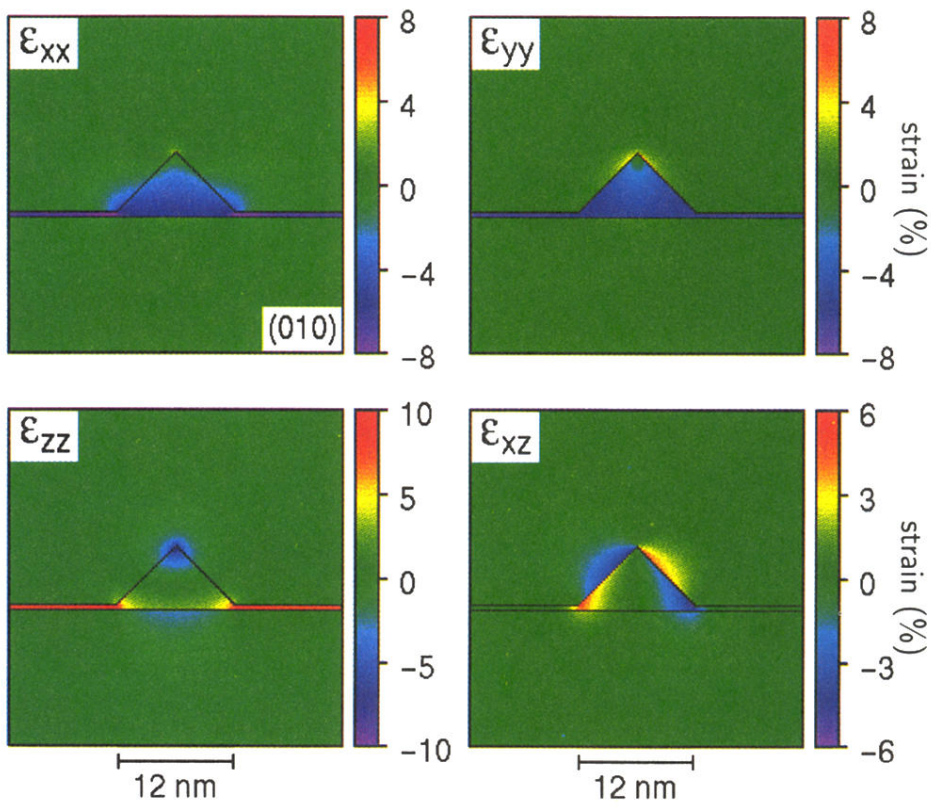


FIG. 3. Strain distribution in the (010) plane through the top of the pyramid.

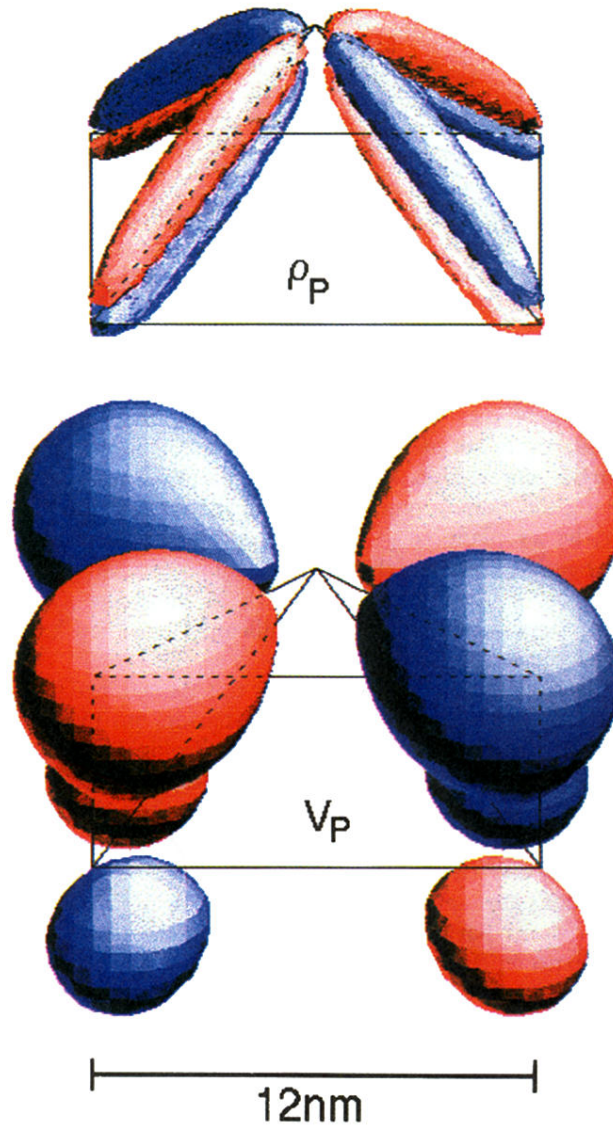


FIG. 8. Upper part: Piezoelectric charge density due to shear strain in a 12-nm QD (isosurfaces for a volume charge density $|q|=0.3 e \text{ nm}^{-3}$). The front left edge is on a $\{112\}A$ surface; thus the outer charge (red) is positive. Lower part: Resulting piezoelectric potential (isosurface for $|V_P|=30 \text{ meV}$). In both parts equal color means equal sign.

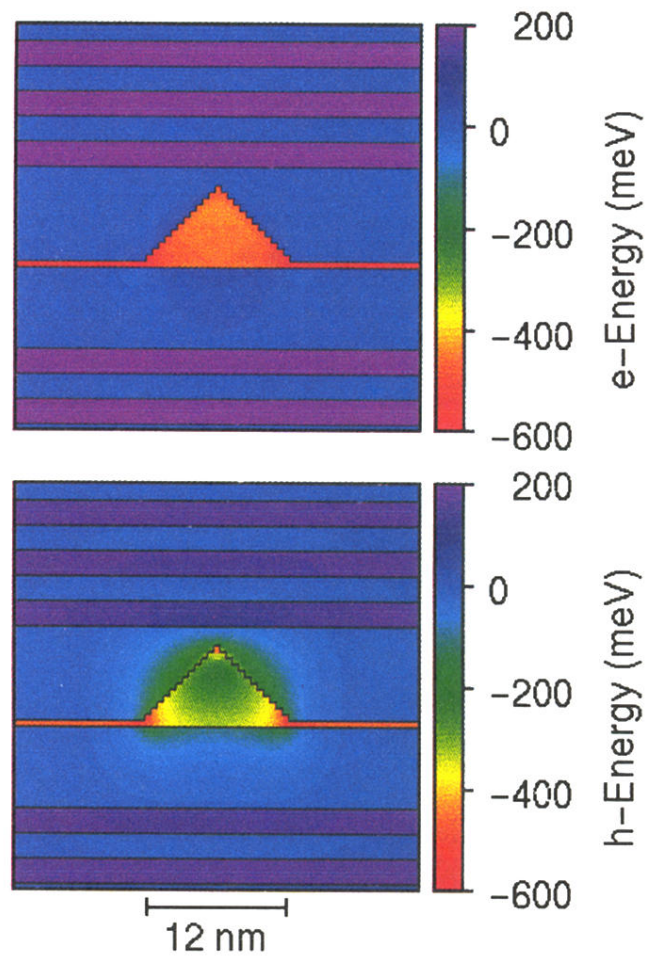


FIG. 9. InAs QD's in GaAs and $\text{Al}_{0.3}\text{Ga}_{0.7}\text{As}$ superlattices. Confinement potential for electrons (top) and holes (bottom), including modification of the band structure due to strain.